JGR Space Physics

RESEARCH ARTICLE
10.1029/2021JA030102

Key Points:

- The Super Dual Auroral Radar Network and the Active Magnetosphere and Planetary Electrodynamics Response Experiment derived Poynting flux (PF) distributions are used to perform a superposed epoch analysis of interplanetary magnetic field (IMF) B_z transitions
- Changes in the IMF B_z component have immediate responses, but continue to evolve for several tens of minutes
- There is spatial and temporal asymmetry to how the PF morphology responds to opposite B_z transitions

Correspondence to:
D. D. Billett,
daniel.billett@usask.ca

Citation:
Billett, D. D., McWilliams, K. A., Perry, G. W., Clausen, L. B. N., & Anderson, B. J. (2022). Ionospheric energy input in response to changes in solar wind driving: Statistics from the SuperDARN and AMPERE campaigns. *Journal of Geophysical Research: Space Physics*, *127*, e2021JA030102. https://doi.org/10.1029/2021JA030102

Received 3 NOV 2021
Accepted 23 FEB 2022

Ionospheric Energy Input in Response to Changes in Solar Wind Driving: Statistics From the SuperDARN and AMPERE Campaigns

D. D. Billett[1], K. A. McWilliams[1], G. W. Perry[2], L. B. N. Clausen[3], and B. J. Anderson[4]

[1]Institute of Space and Atmospheric Studies, University of Saskatchewan, Saskatoon, SK, Canada, [2]Center for Solar-Terrestrial Research, New Jersey Institute of Technology, Newark, NJ, USA, [3]Department of Physics, University of Oslo, Oslo, Norway, [4]Applied Physics Laboratory, Johns Hopkins University, Laurel, MD, USA

Abstract For over a decade, the Super Dual Auroral Radar Network and the Active Magnetosphere and Planetary Electrodynamics Response Experiment have been measuring ionospheric convection and field-aligned currents in the high-latitude regions, respectively. Using both, high-latitude maps of the magnetosphere-ionosphere energy transfer rate (the Poynting flux) have been generated with a time resolution of 2 min between 2010 and 2017. These data driven Poynting flux (PF) patterns are used in this study to perform a superposed epoch analysis of the northern hemisphere ionospheric response to transitions of the interplanetary magnetic field B_z component, upwards of 60° geomagnetic latitude. We discuss the difference in the distribution of PF between the magnetosphere-ionosphere Dungey cycle "switching on" and "switching off" to solar wind driving, revealing that they are not symmetric temporally or spatially.

Plain Language Summary The Earth's high-latitude upper atmosphere (the ionosphere, upwards of 100 km in altitude) is consistently bombarded with solar energy that takes the form of electric currents aligned with Earth's magnetic field. The magnetosphere has two generalized states, "open" and "closed." Open is when the Earth and interplanetary magnetic fields (IMFs) connect to each other on the dayside, allowing energy into the atmosphere from the solar wind. Closed is when the fields do not connect (or do not connect simply) and thus not as much energy enters the atmosphere. The aforementioned open or closed states depend on the direction of the IMF, which varies constantly, as well as the history of the field as the magnetosphere takes time to reconfigure. In this study, we utilize nearly 8 years of data to generate average patterns of ionospheric energy input at various intervals before and after the IMF flips in direction. We discuss the spatial and temporal timescales upon which the energy varies in response to the relatively symmetric IMF transitions, finding that they do not result in symmetric changes in the ionospheric energy input patterns.

1. Introduction

In 2009, the Iridium constellation of satellites began consistently delivering magnetic field data at their orbital altitude of ~780 km to be processed as part of the Active Magnetosphere and Planetary Electrodynamics Response Experiment (AMPERE; Anderson et al., 2014). AMPERE has allowed for the derivation of global-scale perturbation magnetic fields at F-region ionospheric altitudes (at a typical 10-min resolution), which are subsequently processed into patterns of the high-latitude field-aligned currents (FACs). Overlapping with the entirety of the AMPERE data set from its inception to the present day has been consistent measurements of ionospheric plasma flows from the Super Dual Auroral Radar Network (SuperDARN; Greenwald et al., 1995). As of 2021, the SuperDARN consists of 36 high-frequency radars in both the northern and southern hemispheres that are used conjunctively to generate instantaneous patterns of the high-latitude ionospheric convection pattern (Chisham et al., 2007; Nishitani et al., 2019), at a 2-min resolution.

SuperDARN derived convection, or electric potential (Φ), patterns can be converted to the electric field ($\mathbf{E}$) via the relation $\mathbf{E} = -\nabla\Phi$. AMPERE derived perturbation magnetic fields ($\delta\mathbf{B}$) can then be used in conjunction with $\mathbf{E}$ to calculate the total energy transferred between the magnetosphere and ionosphere through FACs, the Poynting flux (PF) ($\mathbf{S}_{\parallel}$), using Poynting's theorem:

$$\mathbf{S}_{\parallel} = -\frac{1}{\mu_0}(\mathbf{E} \times \delta\mathbf{B}) \cdot \hat{\mathbf{r}} \quad (1)$$

where $\hat{\mathbf{r}}$ is the unit vector parallel to the geomagnetic field and μ_0 is the permeability of free space. At the altitude and latitudes where AMPERE data is obtained, the terrestrial magnetic field is essentially vertical and so the measured perturbation magnetic fields are horizontal (Anderson et al., 2000). For the SuperDARN data, perpendicular requirements of the radar signal for ionospheric backscatter mean that only horizontal drift measurements from field-aligned irregularities are possible. Therefore, there is little uncertainty in the parallel field condition for SuperDARN–AMPERE derived PF using Equation 1. Previously, a data set of PF patterns for the northern hemisphere ionosphere has been generated for the entire overlapping AMPERE-SuperDARN datasets between 2010 and 2017 using Equation 1, which has been shown to be consistent with several models and observations (Billett et al., 2021).

This study utilizes the new data set of northern hemisphere PF maps to examine the statistical response of the PF to changes in solar wind driving conditions, primarily after sustained transitions of the Interplanetary Magnetic Field (IMF) B_z component in Geocentric Solar Magnetospheric (GSM) coordinates. These types of IMF transitions are akin to "switching on" ($B_z > 0$ to $B_z < 0$) and "switching off" ($B_z < 0$ to $B_z > 0$) magnetospheric driving of the ionosphere via reconnection at the magnetopause, inducing the Earth's Dungey cycle (Cowley & Lockwood, 1992; Dungey, 1961). Although this is a simplistic view of magnetosphere-ionosphere coupling given that magnetopause reconnection can still occur when the IMF B_z is positive (Onsager et al., 2001), whether the IMF vector is southward ($B_z < 0$) or northward ($B_z > 0$) orientated is the most significant indicator of magnetospheric energy input into the ionosphere (Milan, 2009).

The "switching on" of the magnetosphere-ionosphere driving system (i.e., a positive-to-negative IMF B_z transition) has been extensively studied. For example, the ionospheric electric field is known to respond dynamically to changes in the near-Earth solar wind on the order of minutes (e.g., Murr & Hughes, 2001; Snekvik et al., 2017; Yu & Ridley, 2009). This response begins on the dayside and progresses to the nightside, with the ionospheric electric field fully reconfiguring to a negative B_z orientation within tens of minutes (e.g., Dods et al., 2017; Murr & Hughes, 2001). The global FAC systems finish developing much later, on the order of hours (Coxon et al., 2019). Ionospheric conductivity is also known to play an important role in the rate of FAC formation, contributing to seasonal asymmetries (Coxon et al., 2016).

Negative to positive turnings of the IMF B_z have less commonly been studied. Lobe reconnection under positive B_z results in the development of a new FAC system (NBZ; Iijima et al., 1984), thus lowering the decay rate of the total dayside current and bringing it more in line with the total nightside current decay (Milan et al., 2018). Decay rates are further complicated by the different responses of reconnection driven magnetospheric convection and viscous interaction or flywheel driven convection under positive B_z (Bhattarai et al., 2012). Low nightside conductance may in fact result in faster nightside FAC decay due to weaker line-tying of magnetic field lines (Moretto et al., 2018, 2021).

In this paper, we present the response of the northern hemispheric PF to the aforementioned B_z transitions as a superposed epoch analysis. We discuss how the overlapping SuperDARN and AMPERE data sets were used to do this in Section 2. Results are shown in Section 3, whilst we discuss the differences in how PF increases or decreases depending on the B_z transition in Section 4.

2. Data Processing

Maps of the high-latitude PF were generated for each overlapping AMPERE $\boldsymbol{\delta}\mathbf{B}$ map and SuperDARN convection pattern in the northern hemisphere using the method described by Waters et al. (2004). In short, both $\boldsymbol{\delta}\mathbf{B}$ from AMPERE and $\mathbf{E}$ from the SuperDARN are placed into an equal area (~200 × 400 km) grid poleward of 60° AACGM (Shepherd, 2014) latitude which is also fixed in local time, where each cell has a latitudinal width of 2°. Equation 1 is then used to derive the PF vector on the same grid in AACGM east, north, and field-aligned coordinates. Only the field-aligned component, that is, in the direction of $\hat{\mathbf{r}}$, is used henceforth. All latitudes and magnetic local times (MLTs) mentioned henceforth are referring to AACGM latitude and local time, respectively.

As the global SuperDARN convection patterns are spherical harmonic fits to the plasma velocity data from individual radars (Ruohoniemi & Baker, 1998), a threshold of 200 gridded SuperDARN line-of-sight velocity data points per pattern is imposed before using them to calculate the PF. This ensures there is generally a good spread of real radar velocity data across most local times for any given convection map and reduces the number of

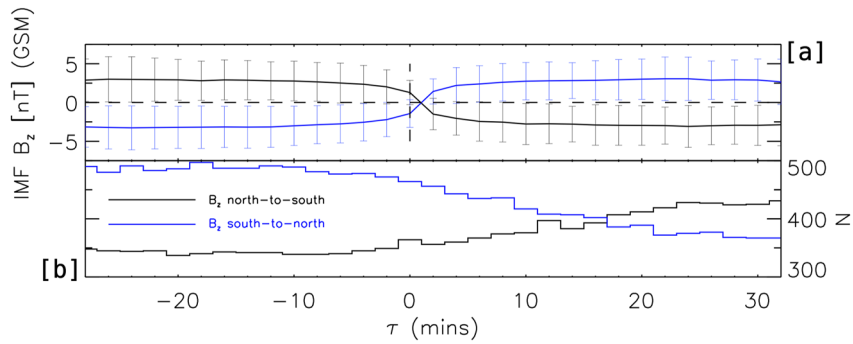

Figure 1. (a) Mean traces of the interplanetary magnetic field (IMF) B_z component during north-to-south (black) and south-to-north (blue) transitions used in this study. Error bars show the ±1 standard deviation of each population. (b) The number of maps meeting the Super Dual Auroral Radar Network data threshold within each epoch for the same transitions shown in (a).

"useable" SuperDARN convection patterns for PF measurements by around 55% (Billett et al., 2018). The SuperDARN radar data are also filtered so that E-region ionospheric backscatter is excluded (by removing data from slant ranges closer than 800 km), giving the convection patterns an assumed F-region altitude of approximately 250 km. Convection patterns use SuperDARN data integrated over 2 min.

The AMPERE data are assumed to be from an altitude of 780 km, which is subsequently scaled to an altitude of 250 km to match the SuperDARN data. This is done using the 3/2 relationship described by Knipp et al. (2014) and results in $\boldsymbol{\delta B}$ being approximately 1.12 times larger than measured. $\boldsymbol{\delta B}$ maps have a 2-min resolution and a sliding 10-min integration window, so when combined with SuperDARN data, PF maps are calculated at a 2-min cadence.

In this study, a superposed epoch analysis of the PF with an epoch spacing of 2 min was carried out for sustained transitions of the IMF B_z component. IMF data are obtained from the 1-min resolution OMNI data set (retrieved from http://omniweb.gsfc.nasa.gov) and is time shifted forward by 10 min to account for the travel of electromagnetic energy between the magnetopause and dayside ionosphere. Ten minutes has been shown to roughly be the average transit time, based on variations in ionospheric flows at a ground-based radar when compared to upstream satellite measurements (Khan & Cowley, 1999).

"Sustained" transitions are defined as intervals where B_z was constantly northward (southward) orientated for at least 30 min prior to becoming southward (northward), upon which the sign of B_z remained the same for an additional 30 min. Using 30 min prior to the transition allows time for the ionosphere to be "settled" under the initial negative or positive B_z by epoch t_0. Thirty minutes after the transition gives a window to examine the directly driven PF response to the IMF change at the dayside magnetopause, which is long enough for the ionospheric electric field to converge to state equivalent to statistical patterns on average (Grocott & Milan, 2014). It is important to note however that 30 min may not be long enough to observe the full ionospheric response due to substorm effects from magnetotail dynamics, which occur on longer timescales in general (~70 min on average; Li et al., 2013). In order to maintain a high number of PF maps for averaging, no B_z magnitude threshold was imposed and the IMF B_y component was not considered.

Figure 1a shows the mean magnitude traces of B_z north-to-south (black) and south-to-north (blue) transitions, versus epoch, for the times used in this study. The average IMF magnitude is consistently around ±2.5 nT both before and after either transition, and the change in magnitude at $\tau = 0$ (t_0) occurs quickly. Figure 1b shows the number of maps meeting the SuperDARN data threshold of 200 gridded vectors within each epoch using the same colors as Figure 1a, indicating that generally more SuperDARN data meets the selection criteria during times of negative B_z.

3. Results

The results of the PF superposed epoch analysis, for sustained north-to-south and south-to-north IMF B_z transitions, are shown in Figure 2. There were 1,301 north-to-south and 1,307 south-to-north transitions during the SuperDARN-AMPERE overlap period, but only PF maps which met the 200 SuperDARN data point threshold

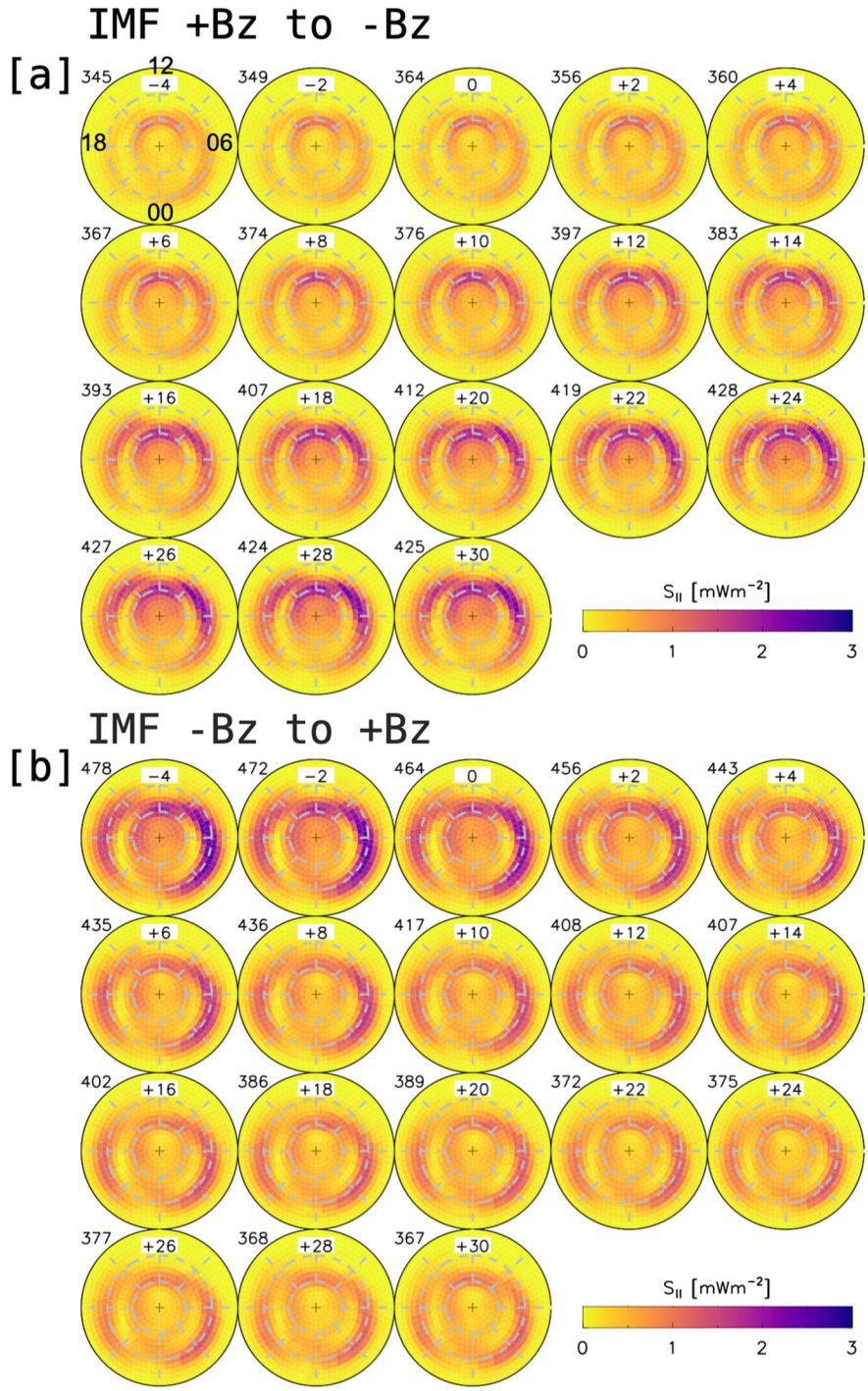

Figure 2. Superposed epoch maps of the downward PF from $t_0 - 4$ to $t_0 + 30$, for (a) north-to-south and (b) south-to-north IMF B_z transitions. Plots are polar projections in AACGM latitude and local time. Noon is to the top and dawn is to the right of each plot. Concentric circles separate 10° of latitude, down to a 60° minimum. Numbers in the top left of each plot denote the number of maps averaged in each epoch.

were used in the average for each epoch (the total in each denoted by the number in the top left of the sub-plots). Data coverage was consistent and not biased toward any specific year or season. The average magnitude of B_y in each epoch was also close to zero.

The patterns shown in Figure 2 are from 4 min prior to the IMF transition to 30 min after in two-minute intervals. Epochs prior to $t_0 - 4$ are not shown here as they do not vary significantly from $t_0 - 4$. Only positive (downward) PFs are shown, as negative (upward) values are nearly always small and thus not perceivable in climatologies. This is to be expected because PF nearly always tends to propagate from the magnetosphere to the ionosphere where it then diverges, not vice versa. We note that more PF maps meet the 200 SuperDARN data point criteria when the IMF is southward, signifying the SuperDARN radars receiving more ionospheric backscatter during more geomagnetically active periods.

For the north-to-south transition in Figure 2a, there are regions of enhanced downward PF that are consistent in their morphology throughout all epochs. These are lower latitude enhancements around 70° latitude on both the dawn and dusk sides, as well as a higher latitude enhancement around 80° latitude centered slightly duskward of noon MLT. Before t_0, the highest PF magnitude is in the high-latitude dayside region (1.2 mW/m^2). From t_0 to $t_0 + 30$, PF gradually increases starting at dayside local times and eventually affecting nightside local times. The largest PF magnitudes at $t_0 + 30$ are located around 80° latitude centered on noon MLT (2.3 mW/m^2), as well as around 70° latitude in the 05–09 and 13–18 MLT regions. PF is noticeably smaller for nightside local times, and very small near midnight (except for polewards of 80° latitude). There is a gradual movement of dawn and duskside enhanced PF equatorward between t_0 and $t_0 + 30$.

In Figure 2b, the IMF B_z south-to-north transition of downward PF is shown. Before t_0, the magnitudes are similar to that in the $t_0 + 30$ epoch of the northward-to-southward transition shown in Figure 2a, but the enhanced dawnside PF extends significantly closer to midnight MLT. At +2 min, there is a steep decrease in PF magnitude when compared to t_0, which is particularly evident in the high-latitude dayside and lower latitude dawnside regions. For example, the PF decreases from a maximum of around 1.8 to 1.3 mW/m^2 at 80° latitude near noon, and from around 2.3 to 1.8 mW/m^2 at 70° near dawn. A similar sharp change after t_0 is not as prominent for the B_z northward-to-southward transition in Figure 2a. At $t_0 + 30$ in Figure 2b, the PF is decreased at all local times relative to the PF at t_0.

To further examine the changes in downward PF magnitudes after the IMF B_z transitions, Figure 3 shows sets of time series plots from 30 min prior to 30 min after a transition. The PF in each bin are first area integrated both above and below 75° latitude, along 24 sectors of magnetic local time, to differentiate between PF variations in the lower and higher latitude regions identified previously. Six local time hours worth of integrated values are then averaged over the nightside (21-03 MLT, red diamonds), dawnside (03–09 MLT, blue squares), dayside (09–15 MLT, yellow circles) and duskside (15–21 MLT, green triangles). The result is the average inbound power over 8 sectors, which we refer to as PF power (PFP), shown in Figure 3.

Figure 3a shows the B_z north-to-south transition for the lower latitude (<75°) region. Prior to t_0, dawnside and nightside PFP is the largest (~0.3 GW), followed by duskside (~0.25 GW) and dayside (<0.05 GW). Dawn and duskside PFP increase after t_0 at a steady rate, to 0.9 and 0.8 GW respectively at $t_0 + 30$, with duskside PFP overtaking the magnitude of nightside PFP. Dayside PFP increases to 0.2 GW after t_0, whilst nightside PFP changes very little.

For the higher latitude (<75°) B_z north-to-south transition (Figure 3b), all regions average a PFP between 0.2 and 0.4 GW before t_0. Dayside PFP is largest and undergoes the most significant increase between t_0 and $t_0 + 30$, up to ~1.1 GW. Dawn and duskside PFP remain comparable as they increase to 0.7 GW, while nightside PFP increases very gradually to 0.35 GW.

In Figure 3c, the B_z south-to-north transition for the lower latitude region is shown. From before t_0 to $t_0 + 30$, dawnside PFP decreases from 1.4 to 0.6 GW, duskside from 1.05 to 0.5 GW, nightside from 0.6 to 0.5 GW and dayside from 0.35 to 0.1 GW. We note that the PFP magnitudes at the beginning ($t_0 - 30$) of the epoch analysis, in particular on the dawn and dusk sides, are larger than corresponding magnitudes at $t_0 + 30$ in Figure 3a (i.e., the reverse B_z transition). This implies that 30 min is not long enough for the PF magnitude to stabilize to the new IMF orientation, which will be commented on further in the discussion section.

Dayside PFP is dominant at high latitudes for the B_z south-to-north transition (Figure 3d), dropping from 1.05 before t_0 to 0.5 GW at $t_0 + 30$. Duskside, dawnside and nightside PFP have lower initial magnitudes of 0.7, 0.6, and 0.5 GW respectively, all decreasing to ~0.35–0.4 GW. We note that for south-to-north B_z transitions (both

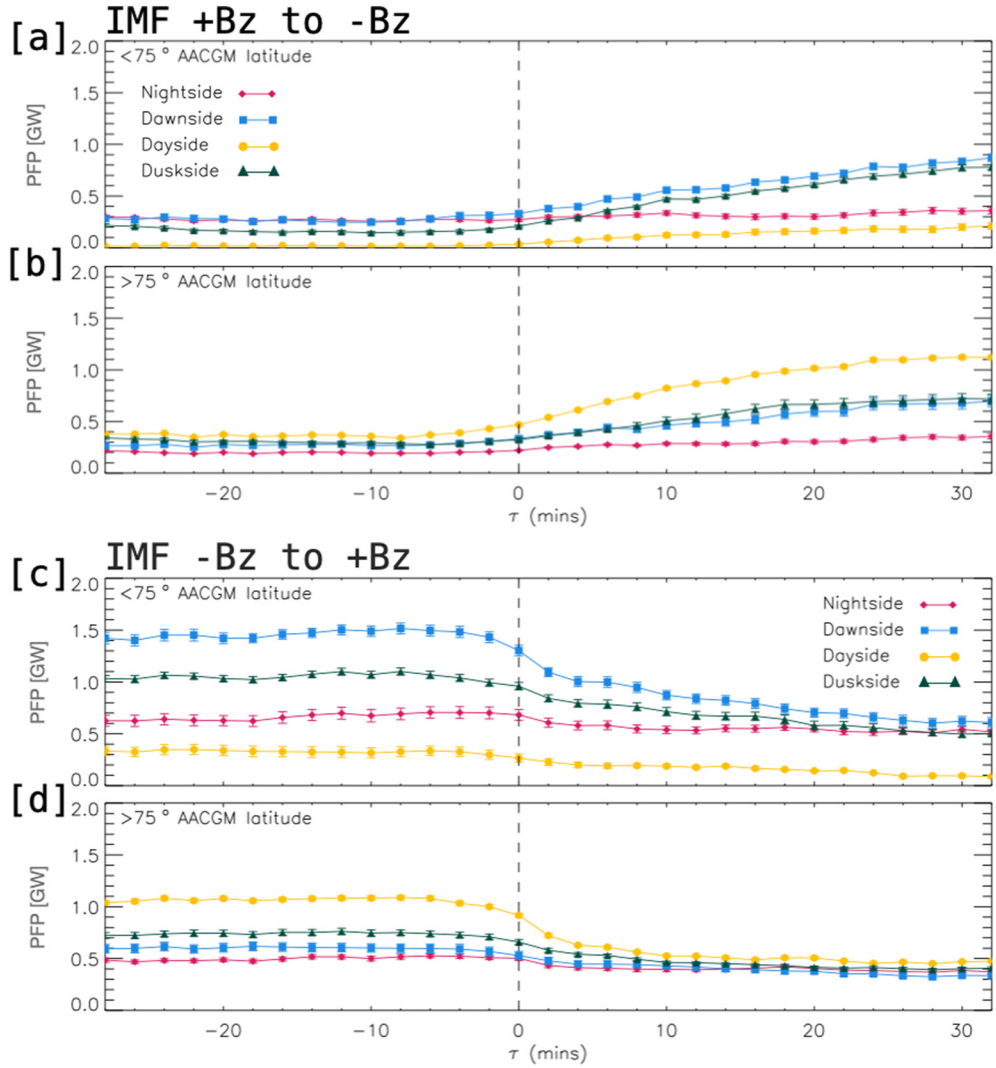

Figure 3. Superposed epoch time series of the downward Poynting flux integrated and then averaged over nightside, dawnside, dayside and duskside local times: (a, b) Northward-to-southward transitions, (c, d) southward-to-northward transitions. Integration is done separately below ([a, c]) and above [b, d]) 75° latitude. Standard errors of the mean are also shown, but are often smaller than the plotting symbols used.

Figures 3d and 3e), the initial PFP decrease after t_0 appears sharper at all local times than the corresponding increase in the north-to-south transition (Figures 3a and 3b).

From Figure 3, it is evident that different local times and latitudinal regions respond at different rates to an IMF B_z transition. In Figure 4, maps of the PF percentage increase (for B_z north-to-south transitions, Figure 4a) and percentage decrease (for south-to-north transitions, Figure 4b) from t_0 are shown. Epochs shown are from t_0 + 2 min to t_0 + 30 min. Only the percentage increase or decrease is shown for respective transitions because on average, the PF does not decrease for B_z north-to-south transitions and vice versa. This is not strictly true for single events and localized regions where very small PF fluctuations can occur in both the positive and negative direction, regardless of B_z transition. Small localized fluctuations, defined as a <0.1 mWm^{-2} increase or decrease from t_0, are however removed from Figure 4. Figure 4 is not meant to illustrate the magnitude of PF changes in certain regions, but more as an indication of the rate of PF change normalized by initial magnitudes at t_0.

In Figure 4a, large percentage enhancements of the PF (+100% or more) within 10 min of the B_z north-to-south transition occur on the dayside and propagate toward the nightside, mainly between 65 and 75° latitude and near the pole. In particular, the post-noon sector PF appears to increase the fastest. The nightside propagation

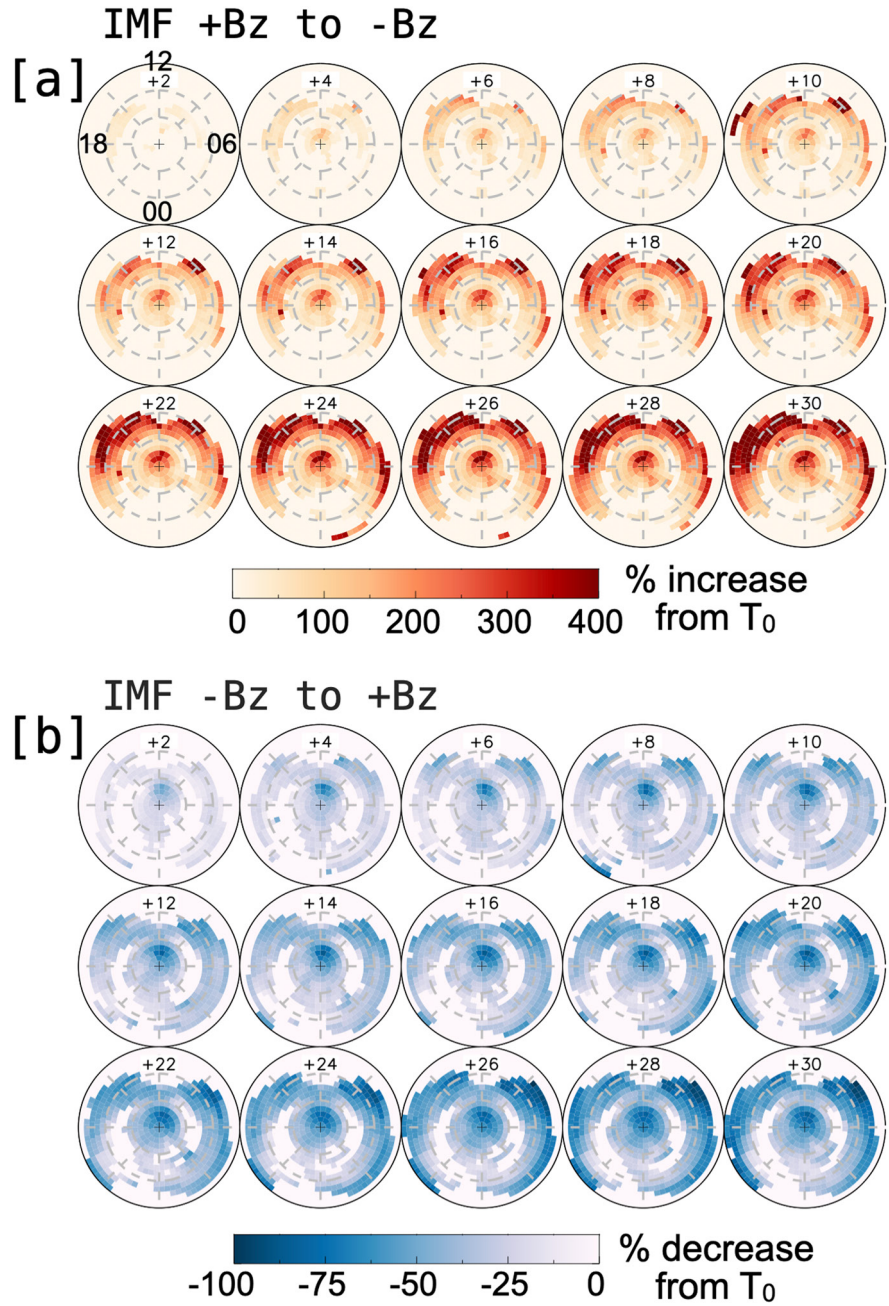

Figure 4. Poynting flux percentage change maps from epoch t_0. (a) Percentage increase after northward-to-southward transitions. (b) Percentage decrease after southward-to-northward transitions.

continues with increasing epoch up to 30 min after the transition, where percentage increases from t_0 reach nearly +400% on the dayside in the post- and pre-noon sectors. There is a clear gradual expansion of the enhancement regions equatorward with increasing epoch, particularly on the nightside a few hours pre- and post-midnight, where there are large percentage enhancements near 60° latitude at $t_0 + 30$.

Within 10 min of a B_z south-to-north transition (Figure 4b), PF percentage decreases of several tens of percent appear to occur both on the day and nightside simultaneously. This initial decrease occurs across most local times and is roughly confined to near the pole (particularly on the dayside), as well as between 65° and 75° latitude on the dawn and dusk sides. PF continues to decrease on the dawn and dusk sides with increasing epoch, decreasing

first at lower latitudes and then later at higher latitudes. By t_0 + 30, PF decreases by as much as 80% at lower latitudes on the dawn and dusk sides have occurred.

4. Discussion

The superposed epoch analysis presented in this study has shown the reconfiguration process of high-latitude PF in response to sign transitions of the IMF B_z component, with a two-minute temporal resolution and a spatial resolution of a few hundred kilometers. The PF patterns shown in this study have a similar general morphology to those in previous studies of PF/Joule heating (e.g., Cosgrove et al., 2014; Knipp et al., 2021; Weimer, 2005) as well as the initial manuscript that introduces this data set (Billett et al., 2021). In short, PF is mostly dissipated around the auroral electrojets, as well as around the dayside cusp at ∼80° latitude. Many previous authors have noted that the high-latitude ionosphere responds almost instantly to IMF changes (e.g., Murr & Hughes, 2001; Ruohoniemi et al., 2002), and we too observe a very fast (<2 min) response of the PF for both north-to-south and south-to-north B_z transitions. The differences between the magnitude of PF before a transition and 30 min after are drastic, but the timescales on which changes occur in local time are gradual and not symmetric for opposite B_z transitions.

We have found that 30 min is not long enough for the morphology of PF to fully reconfigure after an IMF transition, but is long enough to reveal significant asymmetries between the two transitions types shown here. Figures 3a and 3c for example, shows that PFP in the low latitude dawn and dusk sectors do not totally converge to pre-transition magnitudes of the opposite transition. The full PF reconfiguration timescale is thus more likely to be consistent with FAC reconfiguration timescales reported by previous authors (e.g., Anderson et al., 2018; Coxon et al., 2019). Our results are also in agreement with Moretto et al. (2021), in that most of the PF reconfigures within 30 min following a B_z transition. The high-latitude dayside region, the area dominated by PF into the cusp, conversely appears to completely reconfigure within 30 min of a B_z transition. As the cusp region is typically close to the boundary between open and closed (to the solar wind) geomagnetic field lines, the shorter reconfiguration time is perhaps not surprising.

For both B_z transitions, there is a region close to the pole on the dayside that experiences a large percentage increase or decrease in downward PF (Figure 4). This region is on newly opened field lines following a southward transition, and connected to the magnetospheric lobes following a northward transition. The PF magnitude is not particularly large near the pole compared to the main regions of enhancement, but the change that occurs there is drastic probably because the electric field rapidly changes in response to IMF orientation fluctuations. During southward IMF for example, **E** is strongly duskward near the pole (i.e., anti-sunward convection) and starts decreasing within a few minutes following a northward turning (Knipp et al., 1991). The opposite also occurs quickly for the north-to-south transition.

Evident in our analysis is the expanding-contracting polar cap (Cowley & Lockwood, 1992). After IMF B_z north-to-south transitions for example, we can clearly see an immediate increase of the dayside downward PF, followed by increases at local times gradually approaching nightside local times (Figure 4a). This is in agreement with magnetopause reconnection transferring flux into the polar cap and causing it to expand, activating R1 and R2 field aligned currents on the dayside. The lagged expansion of enhanced PF into nightside local times is also consistent with the Cowley and Lockwood (1992) model of purely magnetopause driving, with no magnetotail interaction. This is corroborated by the consistent absence of PF enhancements around midnight up to t_0 + 30 in Figure 4a, and consistent with the long (∼70 min) substorm timescales observed by Li et al. (2013). A future study in this area could focus on PF changes later than 30 min post IMF transition, examining in more depth the dayside-to-nightside morphology changes.

We note that for B_z south-to-north transitions, the decrease of PF at both dayside and nightside local times seems relatively symmetric (Figure 4b), with a slightly faster decrease on the dayside. It would perhaps be expected that the sudden ending of magnetopause reconnection would cause dayside PF to decrease whilst nightside reconnection lingers, causing a lagged nightside response (in line with the ∼30-min reconfiguration times of the ionospheric electric field; Grocott & Milan, 2014). In the modeling by Lockwood and Morley (2004) however, it was observed that the ionospheric electric field decays in a "shape-preserving manner" at all local times after the reconnection voltage decays to zero. Any nightside driven flow already present may indeed continue, but this will also be present at most local times until it eventually decays (e.g., Figure 3b of Cowley and Lockwood (1992)).

The gradual decrease of PF over a 30 min period may also be due to the neutral wind flywheel effect maintaining the ionospheric electric field. That is, after the winds were previously enhanced by ion-neutral collisions (whilst the ionosphere was being actively driven by magnetopause reconnection), they helped to maintain the ionospheric plasma circulation when the IMF turned northward (e.g., Deng et al., 1991) and thus extended the decay time of the PF. Future work in this area could utilize the global-scale coverage of the SuperDARN and AMPERE to investigate PF decay timescales, but would need to be considerate of the complex ionospheric electric and magnetic field variability that may be missed when performing a climatological study.

In addition to the ionospheric electric field, the PF is also controlled by magnetic perturbations from FACs. The ionospheric Pedersen conductance plays an important role in the generation and decay of FACs, thus impacting the decay of PF after the south-to-north B_z transition. A higher conductance can result in slower FAC formation or decay (Moretto et al., 2021), so the lower conductance of the nightside compared to the dayside would result in faster nightside FAC decay. Immediately after a northward transition of B_z however, following the extended period of southward B_z, substorms and the auroral oval may still be active and thus contribute to higher conductance in the nightside auroral zones. Additionally, on the dayside, the generation of NBZ currents following a northward IMF transition impede dayside FAC decay (Milan et al., 2018). After a B_z northward transition, there must be a complicated balance between conductance at various dayside and nightside local times for the PF to decrease roughly at the same rate.

5. Summary

In summary, we have performed a superposed epoch analysis of the high-latitude northern hemisphere PF to changes in the IMF B_z component. The analysis was carried out using ~7.5 years of overlapping SuperDARN and AMPERE data at a 2-min resolution, allowing for a data driven look at how the magnitude and morphology of PF changes when then Dungey cycle is switched "on" or "off." Our key results are that:

1. B_z positive-to-negative and negative-to-positive transitions are not symmetric in how PF increases or decreases. For positive-to-negative, there is a clear dayside-to-nightside progression of the increasing PF. For negative-to-positive transitions, PF decreases simultaneously at most local times, with dayside PF decreasing only slightly faster than that on the nightside
2. Total reconfiguration times of the PF morphology and magnitudes are longer than 30 min, except in the high-latitude cusp region where it is roughly 30 min

It is likely that there is a complicated interplay between ionospheric conductance on the dayside and nightside, which is affecting PF decay rates for B_z negative-to-positive transitions and resulting in the near simultaneous decrease at most local times. For example, lingering auroral activity on the nightside or the formation of NBZ currents on the dayside could be lengthening or shortening field-aligned current decay rates respectively. There is also a potential impact from thermospheric winds, as they could maintain the ionospheric electric field after northward B_z turnings due to the flywheel effect.

Data Availability Statement

SuperDARN data can be downloaded from Globus, instructions of which are provided here: https://superdarn.ca/data-products. SuperDARN data in this study was processed using the Radar Software Toolkit (RST), version 4.5: https://doi.org/10.5281/zenodo.4435297. The AMPERE team and the AMPERE Science Center for providing the Iridium derived data products, which can be plotted and downloaded at: http://ampere.jhuapl.edu/.

Acknowledgments
This research was supported by the National Sciences and Engineering Research Council of Canada (NSERC). DDB was supported by NSERC CREATE Grant #479771-20, whilst KM was supported by NSERC Discovery Grant #RGPIN 05472-2017. The authors

References

Anderson, B. J., Korth, H., Waters, C. L., Green, D. L., Merkin, V. G., Barnes, R. J., & Dyrud, L. P. (2014). Development of large-scale Birkeland currents determined from the active magnetosphere and planetary Electrodynamics Response experiment. *Geophysical Research Letters: Space Physics*, *41*(9), 3017–3025. https://doi.org/10.1002/2014gl059941

Anderson, B. J., Olson, C. N., Korth, H., Barnes, R. J., Waters, C. L., & Vines, S. K. (2018). Temporal and spatial development of global Birkeland currents. *Journal of Geophysical Research: Space Physics*, *123*(6), 4785–4808. https://doi.org/10.1029/2018ja025254

Anderson, B. J., Takahashi, K., & Toth, B. A. (2000). Sensing global Birkeland currents with iridium® engineering magnetometer data. *Geophysical Research Letters*, *27*(24), 4045–4048. https://doi.org/10.1029/2000gl000094

acknowledge the use of data from SuperDARN, an international project made possible by the national funding agencies of Australia, Canada, China, France, Italy, Japan, South Africa, Norway, the United Kingdom and the United States of America. We also thank the AMPERE team and the AMPERE Science Center for providing the Iridium derived data products, which can be plotted and downloaded at: http://ampere.jhuapl.edu/.

Bhattarai, S. K., Lopez, R. E., Bruntz, R., Lyon, J. G., & Wiltberger, M. (2012). Simulation of the polar cap potential during periods with northward interplanetary magnetic field. *Journal of Geophysical Research*, *117*(A4). https://doi.org/10.1029/2011ja017143

Billett, D. D., Grocott, A., Wild, J. A., Walach, M.-T., & Kosch, M. J. (2018). Diurnal variations in global Joule heating morphology and magnitude due to neutral winds. *Journal of Geophysical Research: Space Physics*, *123*(3), 2398–2411. https://doi.org/10.1002/2017ja025141

Billett, D. D., Perry, G. W., Clausen, L. B. N., Archer, W. E., McWilliams, K. A., Haaland, S., et al. (2021). The relationship between large scale thermospheric density enhancements and the spatial distribution of poynting flux. *Journal of Geophysical Research: Space Physics*, *126*, e2021JA029205. https://doi.org/10.1029/2021JA029205

Chisham, G., Lester, M., Milan, S. E., Freeman, M. P., Bristow, W. A., Grocott, A., et al. (2007). A decade of the super dual auroral radar Network (SuperDARN): Scientific achievements, new techniques and future directions. *Surveys in Geophysics*, *28*(1), 33–109. https://doi.org/10.1007/s10712-007-9017-8

Cosgrove, R. B., Bahcivan, H., Chen, S., Strangeway, R. J., Ortega, J., Alhassan, M., et al. (2014). Empirical model of Poynting flux derived from FAST data and a cusp signature. *Journal of Geophysical Research: Space Physics*, *119*(1), 411–430. https://doi.org/10.1002/2013ja019105

Cowley, S. W. H., & Lockwood, M. (1992). Excitation and decay of solar wind-driven flows in the magnetosphere-ionosphere system. *Annales geophysicae*, *10*, 103–115.

Coxon, J. C., Milan, S. E., Carter, J. A., Clausen, L. B. N., Anderson, B. J., & Korth, H. (2016). Seasonal and diurnal variations in AMPERE observations of the Birkeland currents compared to modeled results. *Journal of Geophysical Research: Space Physics*, *121*(5), 4027–4040. https://doi.org/10.1002/2015ja022050

Coxon, J. C., Shore, R. M., Freeman, M. P., Fear, R. C., Browett, S. D., Smith, A. W., et al. (2019). Timescales of Birkeland currents driven by the IMF. *Geophysical Research Letters*, *46*(14), 7893–7901. https://doi.org/10.1029/2018gl081658

Deng, W., Killeen, T. L., Burns, A. G., & Roble, R. G. (1991). The flywheel effect: Ionospheric currents after a geomagnetic storm. *Geophysical Research Letters*, *18*(10), 1845–1848. https://doi.org/10.1029/91gl02081

Dods, J., Chapman, S. C., & Gjerloev, J. W. (2017). Characterizing the ionospheric current pattern response to southward and northward IMF turnings with dynamical SuperMAG correlation networks. *Journal of Geophysical Research: Space Physics*, *122*(2), 1883–1902. https://doi.org/10.1002/2016ja023686

Dungey, J. W. (1961). Interplanetary magnetic field and the auroral zones. *Physical Review Letters*, *6*(2), 47–48. https://doi.org/10.1103/physrevlett.6.47

Greenwald, R. A., Baker, K. B., Dudeney, J. R., Pinnock, M., Jones, T. B., & Thomas, E. C. (1995). Darn/superdarn. *Space Science Reviews*, *71*(1–4), 761–796. https://doi.org/10.1007/bf00751350

Grocott, A., & Milan, S. E. (2014). The influence of IMF clock angle timescales on the morphology of ionospheric convection. *Journal of Geophysical Research: Space Physics*, *119*(7), 5861–5876. https://doi.org/10.1002/2014ja020136

Iijima, T., Potemra, T. A., Zanetti, L. J., & Bythrow, P. F. (1984). Large-scale Birkeland currents in the dayside polar region during strongly northward IMF: A new Birkeland current system. *Journal of Geophysical Research*, *89*(A9), 7441–7452. https://doi.org/10.1029/ja089ia09p07441

Khan, H., & Cowley, S. W. H. (1999). Observations of the response time of high-latitude ionospheric convection to variations in the interplanetary magnetic field using eiscat and imp-8 data. *Annales geophysicae*, *17*, 1306–1335. https://doi.org/10.1007/s00585-999-1306-8

Knipp, D. J., Kilcommons, L., Hairston, M., & Coley, W. R. (2021). Hemispheric asymmetries in poynting flux derived from DMSP spacecraft. *Geophysical Research Letters*, *48*(17), e2021GL094781. https://doi.org/10.1029/2021gl094781

Knipp, D. J., Matsuo, T., Kilcommons, L., Richmond, A., Anderson, B., Korth, H., et al. (2014). Comparison of magnetic perturbation data from LEO satellite constellations: Statistics of DMSP and AMPERE. *Space Weather*, *12*(1), 2–23. https://doi.org/10.1002/2013sw000987

Knipp, D. J., Richmond, A. D., Emery, B., Crooker, N. U., de La Beaujardiere, O., Evans, D., & Kroehl, H. (1991). Ionospheric convection response to changing IMF direction. *Geophysical Research Letters*, *18*(4), 721–724. https://doi.org/10.1029/90gl02592

Li, H., Wang, C., & Peng, Z. (2013). Solar wind impacts on growth phase duration and substorm intensity: A statistical approach. *Journal of Geophysical Research: Space Physics*, *118*(7), 4270–4278. https://doi.org/10.1002/jgra.50399

Lockwood, M., & Morley, S. K. (2004). A numerical model of the ionospheric signatures of time-varying magnetic reconnection: I. Ionospheric convection. *Annales geophysicae*, *22*, 73–91. https://doi.org/10.5194/angeo-22-73-2004

Milan, S. E. (2009). Both solar wind-magnetosphere coupling and ring current intensity control of the size of the auroral oval. *Geophysical Research Letters*, *36*(18), L18101. https://doi.org/10.1029/2009GL039997

Milan, S. E., Carter, J. A., Sangha, H., Laundal, K. M., Østgaard, N., Tenfjord, P., et al. (2018). Timescales of dayside and nightside field-aligned current response to changes in solar wind-magnetosphere coupling. *Journal of Geophysical Research: Space Physics*, *123*(9), 7307–7319. https://doi.org/10.1029/2018ja025645

Moretto, T., Hesse, M., Kuznetsova, M., Rastätter, L., Vennerstrøm, S., & Tenfjord, P. (2021). How does the magnetosphere go to sleep? *Journal of Atmospheric and Solar-Terrestrial Physics*, *220*, 105626. https://doi.org/10.1016/j.jastp.2021.105626

Moretto, T., Hesse, M., Vennerstrøm, S., & Tenfjord, P. (2018). Estimating the rate of cessation of magnetospheric activity in ampere field-aligned currents. *Geophysical Research Letters*, *45*(23), 12–713. https://doi.org/10.1029/2018gl080631

Murr, D. L., & Hughes, W. J. (2001). Reconfiguration timescales of ionospheric convection. *Geophysical Research Letters*, *28*(11), 2145–2148. https://doi.org/10.1029/2000gl012765

Nishitani, N., Ruohoniemi, J. M., Lester, M., Benjamin, J., Baker, H., Koustov, A. V., et al. (2019). Review of the accomplishments of mid-latitude super dual auroral radar Network (SuperDARN) HF radars. *Progress in Earth and Planetary Science*, *6*, 27. https://doi.org/10.1186/s40645-019-0270-5

Onsager, T. G., Scudder, J. D., Lockwood, M., & Russell, C. T. (2001). Reconnection at the high-latitude magnetopause during northward interplanetary magnetic field conditions. *Journal of Geophysical Research*, *106*(A11), 25467–25488. https://doi.org/10.1029/2000ja000444

Ruohoniemi, J. M., & Baker, K. B. (1998). Large-scale imaging of high-latitude convection with super dual auroral radar Network HF radar observations. *Journal of Geophysical Research*, *103*(A9), 20797–20811. https://doi.org/10.1029/98ja01288

Ruohoniemi, J. M., Shepherd, S. G., & Greenwald, R. A. (2002). The response of the high-latitude ionosphere to IMF variations. *Journal of Atmospheric and Solar-Terrestrial Physics*, *64*(2), 159–171. https://doi.org/10.1016/s1364-6826(01)00081-5

Shepherd, S. G. (2014). Altitude-adjusted corrected geomagnetic coordinates: Definition and functional approximations. *Journal of Geophysical Research: Space Physics*, *119*(9), 7501–7521. https://doi.org/10.1002/2014ja020264

Snekvik, K., Østgaard, N., Tenfjord, P., Reistad, J. P., Laundal, K. M., Milan, S. E., & Haaland, S. E. (2017). Dayside and nightside magnetic field responses at 780 km altitude to dayside reconnection. *Journal of Geophysical Research: Space Physics*, *122*(2), 1670–1689. https://doi.org/10.1002/2016ja023177

Waters, C. L., Anderson, B. J., Greenwald, R. A., Barnes, R. J., & Ruohoniemi, J. M. (2004). High-latitude poynting flux from combined Iridium and SuperDARN data. *Annales geophysicae*, *22*, 2861–2875. https://doi.org/10.5194/angeo-22-2861-2004

Weimer, D. R. (2005). Improved ionospheric electrodynamic models and application to calculating Joule heating rates. *Journal of Geophysical Research*, *110*(A5). https://doi.org/10.1029/2004ja010884

Yu, Y., & Ridley, A. J. (2009). Response of the magnetosphere-ionosphere system to a sudden southward turning of interplanetary magnetic field. *Journal of Geophysical Research*, *114*(A3). https://doi.org/10.1029/2008ja013292